

IDH3 γ serves as a redox switch that regulates mitochondrial energy metabolism and contractility in the heart under oxidative stress

Maithily Nanadikar

Universitätsmedizin Göttingen

Ana Vergel Leon

Universitätsmedizin Göttingen

Jia Guo

Universitätsmedizin Göttingen <https://orcid.org/0000-0002-4055-9103>

Gijsbert van Belle

Universitätsmedizin Göttingen <https://orcid.org/0000-0002-2122-8704>

Aline Jatho

Universitätsmedizin Göttingen

Astrid Brandner

Friedrich-Alexander-University Erlangen-Nürnberg

Rainer Böckmann

Friedrich-Alexander University Erlangen-Nürnberg <https://orcid.org/0000-0002-9325-5162>

Shi Rhunzu

Universitätsmedizin Göttingen <https://orcid.org/0000-0003-3266-1623>

Susanne Brodesser

CECAD Research Center <https://orcid.org/0000-0001-5631-0663>

Marlen Schmidtendorf

University of Cologne <https://orcid.org/0000-0001-9003-3380>

Jingyun Lee

Wake Forest School of Medicine

Hanzhi Wu

Wake Forest School of Medicine

Cristina Furdul

Wake Forest School of Medicine <https://orcid.org/0000-0003-3771-7999>

Joseph Burgoyne

Boston University School of Medicine

Ivan Bogeski

Universitätsmedizin Göttingen

Jan Riemer

University of Cologne

Arpita Chowdhury

University of Göttingen

Peter Rehling

Universitätsmedizin Göttingen <https://orcid.org/0000-0001-5661-5272>

Tobias Bruegmann

University Medical Center Göttingen <https://orcid.org/0000-0002-6930-9634>

Vsevolod Belousov

Pirogov Russian National Research Medical University

Dörthe Katschinski (✉ doerthe.katschinski@med.uni-goettingen.de)

Universitätsmedizin Göttingen <https://orcid.org/0000-0003-4630-9081>

Article

Keywords:

Posted Date: May 11th, 2022

DOI: <https://doi.org/10.21203/rs.3.rs-1594117/v1>

License: © ⓘ This work is licensed under a Creative Commons Attribution 4.0 International License. [Read Full License](#)

Abstract

Redox signaling and cardiac function are tightly linked. Still, it is largely unknown which protein targets are affected by H_2O_2 in cardiomyocytes that underly the impaired inotropic effects in oxidative stress. Here, we combined a new chemogenetic mouse model (HyPer-DAO mice) and a redox proteomics approach to identify redox sensitive proteins. Using the HyPer-DAO mice, we prove that increased endogenous production of H_2O_2 in cardiomyocytes leads to a reversibly impaired cardiac contractility *in vivo*. We identified the γ -subunit of the TCA cycle enzyme isocitrate dehydrogenase (IDH)3 as a redox switch and link its modification to mitochondrial metabolism and glutathione synthesis. Microsecond molecular dynamics simulations combined with experiments using cysteine-gene-edited point mutated cells revealed that IDH3 γ Cys148 and 284 are critically involved in H_2O_2 -dependent regulation of IDH3 activity. The oxidative modification of IDH3 γ regulates the competition between energy production by TCA cycle flux and cellular anti-oxidant defense by glutathione synthesis.

Introduction

The term “*oxidative stress*” refers to an imbalance between the production of reactive oxygen species (ROS) and endogenous antioxidant defense mechanisms. ROS consist of molecules that include highly reactive free oxygen radicals and the stable non-radical oxidant (e.g., hydrogen peroxide/ H_2O_2). H_2O_2 is considered to be a chief signaling molecule due to its longer half-life and capacity to diffuse through membranes ¹. An overshoot of H_2O_2 impairs cell function through oxidative damage of proteins and membranes, thereby, inducing cellular dysfunction or death through apoptosis and necrosis ². The redox-modified molecules are mostly affected non-specifically and at random. In contrast to this detrimental function, there is strong evidence that H_2O_2 at low levels can act as specific signal transducers ³. H_2O_2 exerts its effects by reversibly oxidizing protein cysteine thiols (-SH) to sulfenic acid (-SOH) that can finally result in a disulfide bridge formation ⁴. A protein cysteine thiol that can be reversibly oxidized by H_2O_2 is referred to as *redox switch*.

Elucidation of *redox switches* and their regulation provides the basis for a better understanding of the role of redox signaling in health and disease. For the identification of specific redox switches, mass spectrometry (MS)-based redoxome analyses have gained importance ^{5, 6, 7}. These methods allow quantitative and site-specific redox proteomic analyses. They have revealed many different bacterial and eukaryotic proteins, including kinases, phosphatases, transcription factors, and metabolic enzymes that use reversible thiol modifications to rapidly adjust their protein activity to the redox environment of the cell ⁸. Although significantly advanced during the last years, there are still some drawbacks. In many cases studied, the concentrations of H_2O_2 are considerably larger than the concentrations found *in vivo*. In addition, for many of the proteins that were identified to be redox-modified, the consequences of this post-translational modification are still unknown. To understand redox protein targets, redox modifications and their functional integration into the cellular physiology, defined and close to physiological conditions need to be applied. Genetically encoded redox sensors have been developed in the past to detect H_2O_2 levels with high sensitivity ^{10, 11, 12}. These fluorescent protein-based redox probes have important advantages over dyes, such as high specificity, possibility of transgenesis and fine subcellular targeting ¹³. One prime example is the *Hydrogen Peroxide* sensor HyPer that allows real-time monitoring in living cells and tissues ¹⁴. Complementary, chemogenetic tools like the D-amino acid oxidase (DAO) allow a precise and dynamic control of cellular H_2O_2 levels ¹⁵. Previous studies suggest that H_2O_2 is involved in the regulation of cardiac function ¹⁶. However, a conclusive functional mechanism for this relationship is pending. Here, we generated HyPer-DAO transgenic mice that express the H_2O_2 generator and sensor simultaneously and specifically in cardiomyocytes. Phenotyping of the HyPer-DAO mice, together with redox proteomics and cysteine gene editing in a cell model reveal that the γ -subunit of the isocitrate dehydrogenase (IDH)3 acts as a redox switch. Redox-modification of IDH3 γ has profound impact on metabolic adaptation towards increased intracellular H_2O_2 levels and consequently cardiac function.

Results

Generation of cardiomyocyte-specific HyPer-DAO transgenic mice

Chemogenetic tools and biosensors have been proven to be useful in analyzing redox signaling pathways ^{10, 17}. The HyPer-DAO fusion protein offers to stimulate and analyze endogenous H_2O_2 production simultaneously ¹⁸. To apply this tool in an *in vivo* setting, we generated mice that express the HyPer-DAO localized to the nucleus in cardiomyocytes driven by the α MHC promoter (Fig. 1A). We have chosen the nucleus for the expression of the HyPer-DAO fusion protein to create an intracellular H_2O_2 gradient. Successful and tissue-specific expression of HyPer-DAO in the heart of the transgenic mice was verified by Western blot analysis and confocal microscopy of isolated cardiomyocytes (Fig. 1B, C and D). Structurally, the hearts appeared normal (Fig. 1E). The response of the isolated cardiomyocytes towards the DAO-specific substrate D-ala was tested to verify the functionality of the HyPer-DAO fusion protein. Treatment of cardiomyocytes from HyPer-DAO mice with 3–10 mM D-ala resulted in a dose-dependent H_2O_2 response detected by ratiometric measurements of HyPer fluorescence (Fig. 1F). The HyPer fluorescence response was confined to the nuclear compartment and undetectable in the cytosol. Cardiomyocytes did not respond to the stereoisomer L-ala proving the specific function of the overexpressed DAO.

Intracellular H_2O_2 production in cardiomyocytes results in a reversibly impaired inotropic capacity

To understand the functional consequences of intracellular H_2O_2 production, HyPer-DAO mice were fed with 55 mM D-ala or as a control 55 mM L-ala in the drinking water. Seven and 21 days later, we analyzed the response on target RNAs of the redox-sensitive transcription factors NF- κ B and Nrf2 in the hearts of D-ala versus L-ala treated mice (Fig. 2A). NF- κ B and Nrf2 regulate the immune and adaptive cellular responses to oxidative stress, respectively ¹⁹. At low H_2O_2 levels, Nrf2 is induced and transactivates antioxidant enzymes, whereas an intermediate amount of H_2O_2 triggers the activation of NF- κ B and thus an inflammatory response ²⁰. If exceeded, H_2O_2 induces mitochondrial permeability transition pore opening and cell death. We observed a mild activation of the

Nrf2 response reflected by an increase of NQO1, Srxn1 and Txnrd1 RNA levels, whereas the NF- κ B response was almost absent except an increase of iNOS RNA levels in mice after 21 days of D-ala treatment. In line, we found just a minor increase in the RNA levels of the redox-active enzymes Peroxiredoxin (Prdx)1, Prdx2, Prdx5, GPx1, Txn1 and Txn2 excluding a massive activation of inflammation as well as adaptive stress response (**Fig. 2B**). We concluded that the mouse model allows us to study H₂O₂ as a second messenger in cardiomyocytes rather than as a mediator of a non-specific inflammatory oxidative stress response.

We indeed found striking effects of the intracellular H₂O₂ production on cardiac function despite the rather mild oxidative stress response. Ongoing treatment of HyPer-DAO mice with D-ala resulted in a significantly impaired cardiac pump function reflected by a decreased FAS and EF in male (**Fig. 2C**) and female mice (**Suppl. Fig. 1A**). This was not associated with hypertrophy which was demonstrated by unchanged left ventricular anterior and posterior wall thickness. To exclude a transgenic mouse-specific effect, HyPer-DAO mice were also treated with L-ala, which did not induce any significant changes in heart function. Likewise, wild type (wt) mice did not show altered cardiac function after treatment with either D- or L-ala. Interestingly, the H₂O₂-induced impairment of heart function in the HyPer-DAO mice was reversible. The impaired FAS and EF after 7 days of D-ala treatment went back to normal after only two D-ala treatment free days (**Fig. 2D**). A subsequent second 7 days of D-ala treatment again resulted in impaired heart function. After this second impairment, cardiac function still recovered when the D-ala treatment was suspended, although the recovery took longer compared to the response to the first deterioration. Intriguingly, even an impaired contractile function after a longer D-ala treatment, i.e. 21 days, was reversible after 2 days without D-ala (**Suppl. Fig. 1B**). Heart failure is usually relentlessly progressive as the maladaptive processes cause structural changes including fibrotic remodeling²¹. In line with the reversible phenotype after D-ala treatment, we did not detect a significant extent of fibrosis in the left ventricles (**Fig. 2E and Suppl Fig. 1C**). As a positive control for the fibrotic staining, heart sections of mice that underwent transverse aortic constriction were used. H₂O₂-induced impaired inotropic capacity was also evident by a D-ala-induced decrease of force generation in cardiac slices obtained from HyPer-DAO mice compared to wt mice (**Fig. 2F and Suppl Fig. 1D**). The impairment was corrected by pre-incubation of the cardiac slices with N-acetyl-cysteine (NAC), an antioxidant and disulfide breaking agent^{22,23}, which indicates the marred contractility in the HyPer-DAO hearts was at least partially due to cysteine redox modifications.

Redox proteome screen uncovers the mitochondrial IDH3 γ as a H₂O₂ target

To identify specific redox-modified protein targets in the cardiac tissue of HyPer-DAO mice a proteomics approach was performed (**Fig. 3A**). We analyzed left ventricular samples of 7 days D-ala-treated HyPer-DAO tg mice and compared the total reversible oxidation with samples of 7 days D-ala-treated wt mice. The proteomic data revealed nineteen proteins with a significant reduction of reversible oxidation and redox-sensitive cysteine residues in eight proteins with a significant increase in their reversible oxidation (**Fig. 3B and Suppl Tab. 1 and 2**). In the subsequent analysis, we concentrated on the eight proteins with increased total reversible oxidation. Strikingly, mitochondrial proteins were over-represented. This included Prx5. Prxs are a family of thiol peroxidases that scavenge H₂O₂ in cells²⁴. Having found Prx5 demonstrates the validity of the screen performed. Three of the eight identified proteins with significantly increased modification (trifunctional protein β , SDH complex subunit C and IDH 3 γ) are involved in mitochondrial energy production including β -oxidation and TCA cycle activity.

IDHs catalyze an oxidative decarboxylation of isocitrate to α -ketoglutarate²⁵. IDH1 exerts its function in the cytosol and peroxisomes, whereas IDH2 and IDH3 both localize to the mitochondria. IDH1 and IDH2 are homodimers and NADP⁺-dependent enzymes that share considerable sequence similarity (**Fig. 3C**). IDH1 and 2 catalyze the oxidative decarboxylation of isocitrate to 2-ketoglutarate to generate NADPH from NADP⁺ and the reverse reaction i.e. reductive carboxylation of 2-ketoglutarate to isocitrate that oxidizes NADPH to NADP⁺. The forward oxidative decarboxylation reaction plays an important role in cellular defense against oxidative damage by providing NADPH²⁶, the reverse reductive carboxylation reaction is important in several cellular processes, including lipogenesis and glycolysis regulation, through isocitrate synthesis that in turn produces citrate²⁷. By contrast, IDH3 is a hetero-tetramer, composed of two α , one β and one γ subunit, encoded by three independent genes. Unlike IDH1 and 2, IDH3 is NAD-dependent and has a well-established role in the TCA cycle where it catalyzes the irreversible conversion of isocitrate to 2-ketoglutarate while reducing NAD⁺ to NADH²⁸. Reflecting its central role within the TCA cycle, a change in IDH3 activity affects glycolysis and oxidative phosphorylation in several carcinoma cell models²⁹.

IDH3 activity is regulated by a reversible redox modification *in vitro* and *in vivo*

Having found IDH3 γ as a redox-modified protein in the HyPer-DAO mouse model, we next analyzed IDH3 activity in heart lysates of these mice. IDH3 activity was significantly increased in D-ala-treated HyPer-DAO mice compared to their wt littermates (**Fig. 3D**). This effect was specific to IDH3 since neither IDH1 and 2 nor the TCA cycle enzymes SDH, fumarase or malate dehydrogenase were affected. The increased IDH3 enzyme activity was not related to increased IDH3g RNA (**Fig. 3E**) or protein levels (**Fig. 3F**) indicating that the altered enzyme activity was in fact due to the post-translational modification. A reversible modification was further supported by the finding that in 7 days D-ala-treated mice IDH3 activity went back to normal after feeding the animals for 2 days with D-ala free drinking water (**Fig. 3G**). Increased IDH3 activity was likewise detected in cardiomyocytes isolated from HyPer-DAO mice after D-ala treatment *in vitro*, whereas IDH1/2 activity was unaltered (**Fig. 3H**).

To analyze IDH3 redox regulation at cellular level, we created HyPer-DAO HEK cell models. To address cellular compartment-specific effects we generated HEK cells, in which the HyPer-DAO expression was either targeted to the nucleus, the mitochondria or the cytoplasm (HyPer-DAO NLS, HyPer-DAO MLS and HyPer-DAO NES). Correct localization of HyPer-DAO was confirmed by co-staining of the nucleus and the mitochondria followed by confocal microscopy (**Fig. 4A**). All three cell lines responded to stimulation with increasing concentrations of D-ala but not L-ala with a typical HyPer response (**Fig. 4B**). For further analysis we chose a D-ala concentration of 50 mM, which resulted in a similar response in all three cell lines. To analyze how mitochondrial H₂O₂ levels are affected, we transiently overexpressed HyPerRed localized to the mitochondrial matrix in the HyPer-DAO NLS, HyPer-DAO MLS and HyPer-DAO NES cells. Treatment of the cells with D-ala resulted in an increase of H₂O₂ levels in the mitochondria regardless of the original production site of H₂O₂ as detected by simultaneous readings of the HyPer signal localized together with DAO and the HyPerRed signal in the mitochondrial matrix (**Suppl Fig. 2A**). This finding is in line with earlier

experiments demonstrating that H_2O_2 produced in the cytosol quickly diffuses to the mitochondrial matrix, whereas the opposite direction of diffusion is restricted^{30,31}.

Treatment of HyPer-DAO NLS, HyPer-DAO MLS and HyPer-DAO NES HEK cells with 50 mM D-ala for 20 min resulted, similar to the response observed in the heart samples obtained from the HyPer-DAO mice, in an increase in IDH3 activity (**Fig. 4C**). In contrast, IDH1/2, SDH, fumarase or malate dehydrogenase activities were unchanged (**Suppl. Fig. 3**). L-ala treatment did not produce a similar effect. The D-ala-induced increased IDH3 activity was blunted by co-treatment with the antioxidant NAC. To exclude that NAC inhibits the amount of ROS produced in the cells rather than affecting protein redox-modifications, we determined the HyPer response and $\text{O}_2^{\cdot-}$ levels after D-ala treatment. Whereas the HyPer response, which relies on a reversible disulfide bridge formation, was blunted by co-stimulation with D-ala and NAC, $\text{O}_2^{\cdot-}$ levels were unaffected (**Fig. 4D**). An oxidation-dependent IDH3 activity was further supported by the fact that treatment of the cells with a bolus of H_2O_2 produced an effect comparable to D-ala treatment. The effect of D-ala-induced H_2O_2 production on IDH3 activity was the same in the HyPer-DAO NLS, HyPer-DAO MLS and HyPer-DAO NES HEK cells excluding that the primary subcellular production site of H_2O_2 is of importance. Therefore, we concentrated in the following experiments on the HyPer-DAO NLS HEK cells. A cysteine oxidation in IDH3g after D-ala or H_2O_2 treatment was verified in PEG switch assays (**Fig. 4E**). The D-ala-induced increase in IDH3 activity was reversible upon washing off the D-ala (**Fig. 4F**) along with a no longer detectable IDH3g cysteine oxidation under the same condition as well as after treatment with NAC (**Fig. 4G**). To exclude non-specific effects of D-ala, we treated HEK wt cells with D-ala, L-ala and H_2O_2 , from which only H_2O_2 induced an increased IDH3 activity (**Suppl Fig. 4A**).

Stimulation of endogenous H_2O_2 production results in an impaired ATP production in mitochondria

To gain insight into the effects of endogenously produced H_2O_2 on the energy status of the HyPer-DAO NLS cells, we analyzed the consequence of D-ala, L-ala and H_2O_2 treatment on the cellular ATP levels (**Fig. 5A**). ATP levels were significantly decreased in HyPer-DAO NLS cells after treatment with D-ala or H_2O_2 . This effect was partially prevented by co-treatment with NAC. The respective contribution of glycolytically-produced and mitochondria-derived ATP was analyzed by determining the extracellular acidification rate and the oxygen consumption rate, respectively. These assays revealed that mitochondrial and glycolytic ATP synthesis were likewise impaired after D-ala treatment in HyPer-DAO NLS cells (**Fig. 5B**), whereas D-ala treatment had no similar effect on HEK wt cells (**Suppl. Fig. 4B and C**). An impairment of mitochondrial ATP synthesis was also observed in cardiomyocytes isolated from HyPer-DAO mice after treatment with D-ala (**Fig. 5C**). The impaired mitochondrial function was accompanied by changes in the abundance of TCA cycle metabolites in the HyPer-DAO NLS cells (**Fig. 5D and E**). D-ala treatment skewed the metabolite levels resulting in increased intracellular concentrations of pyruvate, citrate, aconitate, glutamate and glutamine as well as decreased concentration of succinate compared to L-ala or non-treated cells. Glutamate and glutamine metabolism become essential for maintaining cellular redox homeostasis in oxidative stress conditions³². Glutamine counteracts H_2O_2 via contributing to glutathione synthesis. Glutathione is a tripeptide (Glu-Cys-Gly) that deactivates radicals and protects cellular thiol proteins by protein S-glutathionylation. Glutamine and glutamate are considered the rate-limiting factors in glutathione synthesis. The ratio of reduced glutathione to oxidized glutathione (GSH/GSSG) was significantly decreased in D-ala treated HyPer-DAO NLS cells (**Fig. 5F**), which was accompanied by a depletion of total glutathione levels (**Fig. 5G**).

Cys148 and Cys284 are key for H_2O_2 -induced changes in IDH3 activity

IDH3y contains in total 6 cysteines from which Cys148 and Cys333 were present in the peptide list obtained in the redox proteomic screen described above. IDH3y Cys148 and Cys333 also appeared in a previously published database that was generated based on quantitative mapping of the *in vivo* mouse cysteine redox proteome³³ (**Fig. 6A**). Both cysteines were found to be oxidized in most of the tissues analyzed in this database, supporting a physiological role for H_2O_2 in regulating IDH3 activity. To further gain insight into the importance of cysteine modification in IDH3y, we applied an internet-based disulfide prediction tool³⁴. A crystal structure of the α/γ heterodimer of human IDH3 in complex with Mg^{2+} , citrate and ADP were used as query protein structure to visualize an anticipated disulfide bond³⁵. The result revealed a close proximity between Cys148 and Cys284, which allows disulfide bridge formation.

To further analyze the consequences of this disulfide bridge on the structure of the enzyme, we performed molecular dynamics simulations. Human IDH3 is known to display enzymatic activity at different oligomerization levels. Namely, the hetero-dimer composed of IDH3a and IDH3g subunits has basal activity, however the hetero-tetramer composed of the dimers IDH3a/g and IDH3a/b has a much higher activity³⁶. Furthermore, the IDH3a/g dimer can be allosterically regulated by citrate and/or ADP³⁵. As shown in **Fig. 6B** the allosteric site is located in the g-subunit, whereas the catalytic site of the dimer is within the a-subunit. In addition, the clasp region is marked in the figure as it defines the tetramer interface, i.e. the interface between the dimers IDH3a/g and IDH3 a/b. We ran 2 sets of 5 simulations of the IDH3a/g dimer in presence of Mg^{2+} , citrate, and ADP. Based on the evidence from the disulfide prediction, one set of simulations included a disulfide bond between Cys284g and Cys148g (SS), whereas the other did not (noSS).

A global root mean square deviation (RMSD) analysis of the simulations separately for the full dimer complex and for the individual subunits revealed that the systems without the disulfide bond are marginally less stable, particularly regarding the a-subunit (**Suppl Fig. 5**). More importantly, the RMSD of the clasp domain of the IDH3a/g dimer indicates that two of the noSS replicas are structurally diverging in that area (**Fig. 6C**); in particular the region spanning residues 149a to 163a, in the vicinity of the catalytically relevant Tyr153a, became unstructured (**Fig. 6D**). This conformational change particularly affects the tetramerization interface (depicted in blue) as compared to the reference simulations in presence of the disulfide bond (depicted in cyan). In order to systematically identify the differences related to disulfide bond formation (i.e. between systems noSS and SS) we performed a force distribution analysis³⁷. **Fig.6E** shows the residue-based stress difference (noSS - SS). The main residues with statistically significant changes in the stress profile are highlighted. Substantial differences are seen within the vicinity of Tyr153a with residues Glu150a and Glu152a (both at the beginning of the first β -sheet of the a subunit's clasp). Other residues were found close to the disulfide region such as Ile163g (β -sheet in contact with S-S bridge, part of the rigid core of g-subunit) and Tyr174g (loop before clasp of g-subunit) and Ile279g which lies on the same α -helix as Cys284g. A region with significant increase in the overall stress upon removal of the disulfide bond is found at the apical domain of the g-subunit, in vicinity of its termini (*tan* sticks in **Fig. 6E**). From a functional point of view, the N-terminal region of the g-subunit has been shown to interact with the b-subunit cleft within the octameric conformation of IDH3³⁸. The stress patterns overall

suggest a stress transfer from the region of the disulfide bond towards the clasp domain that might affect the tetramerization interface as it mainly implies changes on the β -sheets of the clasp domain that do not directly contribute to the dimerization interface but rather are part of the tetramerization interface.

H₂O₂-dependent IDH3g Cys148 modification regulates the competition between energy production by TCA cycle flux and cellular anti-oxidant defense by glutathione synthesis

To analyze the functional importance of the results obtained in the molecular simulation, IDH3g Cys148 and Cys284 were gene edited to alanine in HyPer-DAO NLS HEK cells (HyPer-DAO C148A and HyPer-DAO C284A). Basal IDH1/2 and IDH3 activities in the gene-edited cells were not significantly different compared to the HyPer-DAO NLS wt cells (**Fig. 7A and B**). Treatment of the cells with D-ala however demonstrated that the H₂O₂-induced increase of IDH3 activity was abolished in the C148A and C284A cells. To exclude a non-specific effect of the cysteine mutation, we also gene edited IDH3g Cys236 to alanine (HyPer-DAO C236A). The C236A cells responded to the D-ala treatment similar to the wt cells with an increased IDH3 activity. The non-responsive IDH3 activity in the C148A and C284A cells after D-ala treatment was accompanied by a loss of cysteine oxidation as detected by PEG switch assay in the C148A but not the C284A mutant (**Fig. 7C**). Thus, IDH3g Cys148 might act as the redox-active, peroxidatic cysteine, which is first oxidized and subsequently attacks Cys284 for disulfide binding. We further went on to characterize the metabolism in the wt compared to the C148A mutant cells. The abolished effect of H₂O₂-induced increase of IDH3 activity in the C148A cells was associated with a rescue of mitochondrial ATP production after D-ala treatment. This was seen by analyzing oxygen consumption rates as well as by employing a mitochondria-specific fluorescent ATP fluorescent dye (**Fig. 7D and E**). Whereas ATP levels and the oxygen consumption rate dropped in the HyPer-DAO NLS wt cells after D-ala treatment, this impairment was no longer observed in the C148A cells. Glycolytic ATP production, however, was still impaired in the Cys148 gene edited cells after D-ala treatment alike in the HyPer-DAO wt cells. This demonstrates that IDH3g Cys148 and Cys284 are crucial for mediating the oxidation-induced mitochondrial metabolic changes but not the change in glycolytic ATP production. Consistent with the altered IDH3 activity and rescued mitochondrial ATP levels in the C148A cells, TCA cycle intermediates were generally elevated in the mutated cells compared to the wt cells (**Fig. 7F**). This points to an overall higher TCA cycle activity. As demonstrated above, citrate and aconitate levels were increased in the HyPer-DAO NLS wt cells after D-ala treatment. This effect was not observed in the C148A cells. The changes in TCA cycle intermediates were accompanied by an aggravated depletion of total glutathione levels in the C148A compared to the wt cells (**Fig. 7G**). Overall, the data demonstrate that IDH3g Cys148 oxidation under oxidative stress is important for balancing mitochondrial ATP production by TCA cycle flux and anti-oxidant activity by glutathione levels.

Discussion

H₂O₂ was long regarded as a non-specific damaging agent. This notion has shifted to recognizing its specific role in cell biology^{39,40}. The conceptual change was in part triggered by the development of MS-based proteomic methods that reliably quantify protein oxidative modifications in cell and tissue samples⁴¹. Proteome-wide analysis of cysteine oxidation revealed regulatory post-translational modifications. It is well recognized that alterations of the redox balance towards oxidation is associated with various pathological conditions, including cardiovascular diseases, diabetes, cancer, asthma, neurological disorders and ageing⁴². To gain a better understanding of specific protein targets affected by H₂O₂ in these diseases, the development of relevant cell and animal models is important. We used a newly generated chemogenetic mouse model in combination with MS-based proteomics. A similar chemogenetic approach including DAO was applied before in a rat model, in which rats were treated with a cardiotropic adeno-associated virus expressing HyPer-DAO under control of the cardiac-specific cTnT promoter⁴³. The animals developed a cardiomyopathy and changes in the cardiac metabolome after D-ala treatment⁴⁴. DAO stimulation induced a classical Nrf2 and NF- κ B response including the induction of the respective target genes in these rats, which is of striking difference to our mouse model and might be due to a much longer (4–7 weeks compared to a maximum of 3 weeks in this study) treatment and an 18-fold higher D-ala concentration applied. Redox-target proteins were not reported in the rat model. Using tissues of the transgenic mice revealed the TCA cycle enzyme IDH3 as a specific H₂O₂ target protein in our study. In detail, the γ -subunit of IDH3 was identified as a reversible redox switch demonstrating that H₂O₂-signaling and metabolism converge at the TCA cycle. The α and β -subunits of IDH3 as well as the IDH1 and IDH2 isoforms were unaffected. The γ -subunit has regulatory function for the activity of the IDH3 tetramer and the redox modification identified in our mouse and cell models indeed results in altered enzyme function. There is some evidence from non-mammalians that IDH enzymes are redox modified. In contrast to mammals, most bacteria and archaea however contain only NADPH-dependent homologues of IDH1/2. Inactivation of the prokaryote *Azotobacter vinelandii* NADPH-dependent IDH enzyme was related to thiol group modifications⁴⁵. Inactivation of the NADPH-dependent IDH homologue was similarly observed in *Capsicum annuum*⁴⁶ and *Arabidopsis thaliana* after incubating the recombinant protein with nitroso-glutathione⁴⁷. A redox-modification of IDH3 and its role in mammalian metabolism has not been described so far.

Mitochondria have their own specific thiol redox machineries⁴⁸, which overall could promote specific and reversible thiol modifications. Mitochondrial-derived ROS affect multiple cellular functions⁴⁹. In addition, it is well-established that redox regulation of mitochondrial protein thiols is important for their function⁵⁰. Aside from thiol-oxidation this includes S-nitrosation, which has been described to induce protection of the ischemic myocardium (Chouchani et al., 2013). Within our redox proteomic screen, we identified several mitochondrial protein candidates that demonstrated increased redox modification upon stimulation of endogenous cellular H₂O₂ production including TCA cycle enzymes. The TCA cycle is the principal means of aerobic energy metabolism from acetyl-CoA. A number of mammalian enzymes in the TCA cycle and the oxidation phosphorylation pathway have been shown to be redox-modified in the past. This includes the 2-oxoglutarate dehydrogenase⁵¹, aconitase⁵² and complex I, II and V^{53,54}. Succinate dehydrogenase complex subunit C, which is one of four nuclear-encoded subunits that comprise complex II, was also in the candidate list in our redox proteomics screen. Analysis of SDH activity, however, revealed no change after D-ala treatment in our mouse or cell models. Redox modifications due to an increase in H₂O₂ levels are typically described to result in decreased activities of these enzymes. In consequence, this diminishes NADH production and therefore limits electron flow and thus further ROS release at the cost of ATP synthesis. This seems to be part of the pathophysiological events during ischemia-reperfusion injury⁵⁵. By profiling NF- κ B and Nrf2 target genes, we could show that the oxidative stress was mild in our mouse model. This might explain why we did not see a decrease in SDH activity, although the enzyme

was affected by redox modification. In contrast to the mostly inhibiting effects by redox modification described so far, we found a gain of function in IDH3 in consequence of thiol modification. These functional analyses were paralleled by molecular simulations and analyses of cysteine point mutated cell lines. Altogether these data imply that IDH3γ Cys148 and Cys284 build a reversible disulfide bridge that favors conformational changes in the catalytically active IDH3α-subunit. Analysis in the IDH3γ C148A point mutated cells indicate that the disulfide bridge and resulting increased IDH3 activity is important for the reversible H₂O₂-induced changes in mitochondrial ATP production. The altered IDH3 activity was found to be reversible upon removal of the H₂O₂ stimulus or by treatment with NAC. These effects were paralleled by a rescued function of the heart and ionotropic capacity of myocardial slices under the same conditions. Detrimental, non-reversible effects of ROS on mitochondrial function described previously were mostly identified by using either exogenously applied H₂O₂, in consequence of a shifted GSH/GSSG ratio or in the setting of ischemia re-perfusion⁵⁶. In contrast, our chemogenetic approach allowed us to analyze the consequences of spatiotemporal fluctuations in locally produced H₂O₂. Our data indicate a link between redox signaling, mitochondrial oxidative metabolism and intracellular glutathione levels upon changes in intracellular H₂O₂ gradients. The on-off characteristic in IDH3 activity in response to H₂O₂ arms cells with a regulatory mechanism that allows metabolic adaptation to changes in the redox environment. Glutathione is the major cellular antioxidant combating oxidative stress⁵⁷. Whereas the glutathione pool can shuttle reversibly between GSH and GSSG, increased oxidative stress results in depletion of the overall pool. Therefore, glutathione synthesis becomes crucial for maintaining the cellular antioxidant capacity. Since glutamate and glutamine are both important precursors of glutathione, their metabolism can impact on the total glutathione levels. Glutamine and glutamate, however, are likewise important for replenishing the TCA cycle and thus for mitochondrial bioenergetics. Our data indicate that IDH3 seems to support the flux of TCA cycle metabolites to replenish the glutamate and glutamine pool. Metabolic competition between mitochondrial energy production and glutathione synthesis as seen in our cell model in consequence of increased H₂O₂ levels might therefore reflect an adaptive response towards increased oxidative stress. A balance of rerouting glutamine towards the TCA cycle and glutathione synthesis has also been suggested to be part of hepatocellular tumorigenesis (Tompkins et al., 2019).

The physiological importance of the specific and reversible effect of H₂O₂ on IDH3γ was reflected by the fact that the D-ala-treated myocardium retained its ionotropic capacity within two D-ala treatment free days. The notion that endogenous H₂O₂ production did not produce a permanent phenotype was further underscored by the lack of cardiac fibrosis in D-ala-treated mice. This characteristic is similar to post-ischemic myocardial dysfunction also named stunning⁵⁸. Stunned myocardium suffers from a transient and reversible myocardial contractile dysfunction induced by acute ischemia wherein the blood supply is almost completely restored on reperfusion. H₂O₂ was thought for long to play a major causative role in the stunned myocardium⁵⁹. The exact mechanism whereby H₂O₂ depresses contractile function remains speculative and still represents one of the major unresolved issues pertaining to the pathogenesis of myocardial stunning. Using the HyPer-DAO mice, we prove that in conscious mice stimulation of endogenous production of H₂O₂ leads to a stunning-like phenotype associated with specific changes in cellular metabolism and the glutathione pool. We further deliver IDH3γ as a direct molecular target of H₂O₂, which results in a competition between TCA cycle flux and glutathione synthesis.

Methods

Generation of HyPer-DAO transgenic mice

The maMHC-HyPer-DAO-NLS-hGHPolyA plasmid was linearized with the restriction enzyme EcoRV (Thermo Fisher). The linearized plasmid was purified with the Monarch DNA purification kit (New England Biolabs). Transgenic mice were generated by pronuclear blastocyst injection in C57Bl6N mice (Jackson Laboratories). The injection was performed by the Core Facility of the Max Planck Institute for Experimental Medicine, Göttingen. Both adult male and female mice (at the age of 8–14 weeks) were used for the experiments. All the animal work was confirmed by the institutional guidelines and was approved by the Niedersächsische Landesamt für Verbraucherschutz und Lebensmittelsicherheit (33.9-42502-04-16/2352). Mice were genotyped by a standard polymerase chain reaction using the following primers: 5'-CCTGAGACCCGCCAGGAGAG-3' and 5'-GGATCGCTCTCCCTAGCTGC-3', resulting in a 254-bp fragment. Transgenic mice were mated with wt mice to produce heterozygous offspring and wt littermate controls.

D/L-ala treatment of mice

D-alanine (D-ala) and L-alanine (L-ala) were purchased from Sigma-Aldrich. 55 mM D-ala or L-ala were used in the drinking water for the mice in the *in vivo* experiments. The drinking water was exchanged every second day.

Echocardiography

Left ventricular dimension in systole and in diastole, fractional area shortening, anterior and posterior wall thickness, and ejection fraction were measured by transthoracic echocardiography as described^{60,61}. In brief, mice were anesthetized using an induction chamber with a flow of 3% isoflurane (Forene, Abbvie) in presence of oxygen, followed by 1% isoflurane maintained with a face mask on the measurement table. Two-dimensional image tracings were recorded from the parasternal long- and short-axis view at midpapillary level, M-mode was acquired in the short-axis view (Vevo 2100 system, Visual Sonics Inc, Toronto, Canada).

Force measurement

Mice were killed by cervical dislocation and hearts were explanted, retrogradely flushed with ice-cold PBS and the ventricles placed in ice-cold slicing buffer (140 mM NaCl, 6 mM KCl, 1 mM MgCl₂, 1 mM glucose, 10 mM Hepes, 5 mM BDM, pH 7.4). The left ventricle was cut along the middle of the septum and embedded in 4% low-melting agarose (Sigma-Aldrich, USA). 300 μm thick slices were cut. Out of these slices 0.5 cm² tissue squares were prepared, glued (histoacryl glue, B. Braun, Germany) on two plastic triangles and placed into vertical 20 ml glass organ baths filled with 37°C Krebs solution bubbled with carbogen (95% O₂ and 5% CO₂). Plastic triangles were fixed to the hooks of FT20 transducers and core holders with field stimulation electrodes (Hugo Sachs Elektronik, Germany) on each site and pre-stretched to 2-3 mN. Isometric force was measured with a KWS 3073 bridge amplifier (HBM, Germany) and recorded

with a Powerlab 8/35 using the LabChart7.2 software (ADInstruments). Electrical pacing was performed with a Myotronic stimulator (Myotronic) at 0.5 Hz until diastolic force and force generation stabilized. Finally, the pre-stretch was readjusted to 2-3 mN, the pacing frequency was increased to 2 Hz and the experiments started after an additional 15-20 min. Indicated slices were pre-incubated with 1 mM NAC for 15 min and D-alanine (0.1 mM, 1 mM, 10 mM) was added in a 15 min long step. To quantify isometric force, 10-15 peaks without arrhythmic events at the end of each 15 min step were averaged. These values were normalized to the highest force generated by each slice.

Sirius Red/Fast Green

Sections were incubated with a dye combination of Sirius Red and Fast Green (Chondrex) for 30 min. Sections were washed with ddH₂O and dehydrated with ethanol (EtOH 60% 2 min, EtOH 75% 2 min, EtOH 96% 2 min, EtOH 99% 2 min). After mounting (Rotihisto kit II, Roth), sections were analyzed using the Observer D1 microscope (Zeiss). Image J-win64 was used for alignment of the multi-tile images (linear blending, regression threshold: 0.30, overlap settings: 20%). The percentages of total, perivascular and interstitial fibrosis were compared to the total amount of tissue within an image by determining the total tissue areas occupied by cardiomyocytes and collagen but excluding the lumen (i.e., empty spaces). The original images were converted to an RGB stack. The area occupied by tissue was selected and the threshold was applied to delineate the fibrotic area over the entire area.

Proteomics and Redox Proteomics

Tissue homogenization and protein extraction. Heart tissue (10 mg) was homogenized using a Bead-Ruptor (3 cycles, 20s/cycle), followed by addition of 500 µL modified RIPA buffer (mRIPA; 50 mM Tris HCl, 150 mM NaCl, 1 mM EDTA, 1% NP-40, 0.25% sodium deoxycholate, 1 mM NaF) supplemented with 10 mM MSTP ((4-(5-methanesulfonyl-[1,2,3,4]tetrazol-1-yl)-phenol); Xoder Technologies) to selectively block reduced thiols⁶². After 30 min incubation on ice, the tubes were centrifuged at 18,000 g and 4 °C for 10 min, the supernatant was transferred to a new tube and the protein concentration was measured using the bicinchoninic acid (BCA) assay. 100 µg protein fraction was precipitated with 4x cold acetone (volume) overnight at -20°C.

Reduction of reversible oxidized thiols. The protein pellet was isolated by centrifugation at 16,000 g at 4 °C for 5 min, resuspended in 150 µL buffer (50 mM HEPES, 1 mM EDTA, 0.1% SDS, pH 7.5), and reduced using 10 mM DTT (final concentration). Following incubation at 37 °C with shaking (850 rpm) for 1 h, the excess DTT was removed by passing the protein extract through a Bio-Gel P6 spin column.

Enrichment of thiol-containing proteins. Proteins containing newly released thiols were isolated by covalent binding (4°C with up and down rotation overnight) to thiopropyl sepharose resin preconditioned with the binding buffer (50 mM HEPES and 1 mM EDTA, pH 7.5). To remove the non-covalently bound proteins, the resin was washed five times with each of the following solutions: 8 M urea, 2 M NaCl, 0.1% SDS in PBS, 80% (vol/vol) ACN and 0.1% (vol/vol) TFA, and 50 mM NH₄HCO₃.

On-resin tryptic digestion and elution of enriched cysteine-containing peptides. Proteolytic digestion was performed on the resin by adding 200 µL 50 mM NH₄HCO₃ and trypsin (trypsin: protein=1:20; Pierce Trypsin Protease, MS Grade, Thermo Scientific) and overnight incubation at 37°C. After digestion, the resin was similarly washed with 8 M urea, 2 M NaCl, 80% ACN and 0.1% TFA, and 50 mM NH₄HCO₃, and the covalently bound peptides were eluted by incubating three times with 20 mM DTT in 25 mM NH₄HCO₃ and shaking at 850 rpm for 30 min at room temperature. Each eluent was collected by spinning at 1,500 g for 1 min at room temperature. Finally, the resin was washed with 100 µL of 80% ACN/0.1% TFA to collect the residual peptides. The eluent fractions were combined, dried using SpeedVac, and stored at -80 °C until LC-MS/MS analysis.

LC-MS/MS analysis and database search. Dried peptides were dissolved in water containing 0.1% formic acid and 5% ACN. A system consisting of nanoLC (Dionex Ultimate 3000) coupled to a LTQ Orbitrap Velos Pro (Thermo Scientific) was used for analysis. The flow rate was set to 300 nL/min and the peptides were eluted with a 2 hrs linear gradient of solvent A: 95% H₂O, 5% ACN, 0.1% FA, and solvent B: 20% H₂O, 80% ACN, and 0.1% FA. The MS spray voltage was set to 1.9 kV and the temperature of the heated capillary was 300°C. The analysis was performed using top-10 data-dependent MS and MS/MS acquisition in positive ion mode with dynamic exclusion enabled. MS data were processed using Proteome Discoverer v2.2 (Thermo Scientific, Waltham, MA) with the following search engine and parameters: Sequest HT and UniProt mouse protein FASTA database; parent mass error tolerance of 10 ppm; fragment mass error tolerance of 0.6 Da (monoisotopic); maximum missed cleavage with trypsin at 2 sites; variable modifications of +15.995 Da (oxidation) on methionine, and +160.039 Da (MSTP) on cysteine. The identified peptides were validated using a reversed database search with target decoy PSM validator node under the parameters of 0.05 for maximum delta Cn, 0.01 and 0.05 for each strict and relaxed target FDR.

Isolation of cardiomyocytes

Adult ventricular cardiac myocytes were isolated via the Langendorff perfusion as described previously⁶⁰.

Generation of stably transduced cell lines

HEK cells expressing the Hyper-DAO fusion protein in the nucleus (NLS), the cytoplasm (NES) and in the mitochondria (MLS) were generated by lentiviral transduction using pCMVpL4-HyPer-DAAO-3xNLS, pCMV-pL4-HyPer-DAAO-1xNES and pCMV-pL4-HyPer-DAAO-Cox8MLS, respectively. Viral particles were produced in HEK293T cells using the ViraPower lentiviral packaging mix according to the manufacturer's instructions (Thermo-Fischer Scientific). 300 ng/mL puromycin (Sigma-Aldrich) were used to select HEK cells which were successfully integrated with the plasmid. A monoclonal cell population was selected for each cell line by limiting dilution (4 cells/mL).

Gene editing

Single guided RNAs (sgRNAs) were designed using the online tool CRISPOR (<http://crispor.tefor.net/>). The homology-directed repair (HDR) templates for each point mutation were designed as single-stranded oligodeoxynucleotides (ssODNs) along with silent mutations at the PAM sites. sgRNAs and HDR templates were ordered as Alt-R™ Oligos from Integrated DNA Technologies. Cas9 nuclease, HDR enhancer and electroporation enhancer were purchased through Integrated DNA Technologies. Following sequences were used: sgRNA, Cys148: 5'-CGCCTGGAAGGCTCTTACAG-3', sgRNA Cys 284 5'-CATCGTCAACAATGTCTGCG-3', sgRNA Cys236: 5'-CCACCTCCCTGCAGCACTGG-3'; HDR template Cys148: 5'-CTCCCGGACAATGAGGATGTCTATGTCTTGTGCCGGGTCAACACGCTGGAAGGCTCTTGGCGTGAATGACGTTGGCATAGAGGTCCAGGCTGGTGCTGGGAGGGGA 3', HDR template Cys284: 5'-CCCCAGCAGTTTGATGTCATGGTGATGCCCAATCTCTATGGCAACATCGTCAACAATGTCGCCGCTGGACTGGTGGGGGCCAGGCCTTGTGGCTGGGGCCAACTATG 3', HDR template Cys236: 5'-CTGGTGTCTATTCTTAACCCCCACCAGGAACTGGGCGATGGGCTTTTTCTCCAGTGCGCCAGGGAGGTGGCAGCCCGCTACCCTCAGATCACCTTCGAGAACAT 3'. Each sgRNA was prepared by duplexing Alt-R CRISPR-Cas9 crRNA and Alt-R CRISPR-Cas9 tracrRNA. The ribonucleoprotein (RNP) was made by adding Alt-R S.p. Cas9 Nuclease V3 (Integrated DNA Technologies). Cells were electroporated with 5 µL RNP complex, 1.2 µL HDR donor oligo, 1.2 µL Alt-R Cas9 Electroporation Enhancer, and 2.6 µL PBS using the 4D-Nucleofector module of 4D-Nucleofector (Lonza, AAF-1003X) according to the manufacturer's specifications. Single cell colonies were selected and expanded. Genomic DNA was isolated and the successful gene editing in IDH3g was confirmed by Sanger sequencing.

HyPer measurements

For HyPerGreen measurements cells were excited at 420 and 500 nm and the emitted light was recorded at 510 nm using the IX83 microscope and the MT20 illumination system (Olympus). Light intensity was set to 11% for isolated cardiomyocytes, 4% for HEK cells and the exposure time was set to 1 sec. Each image was recorded at an interval of 120 sec. After reaching stable baseline readings, D-ala, L-ala or H₂O₂ were added respectively. In some experiments stably transduced HEK cells were transiently transfected with pC1-HyPerRed-mito plasmid ⁶³ by lipofection, cells were excited at 590 nm and the emitted light was recorded at 605 nm.

MitoSOX measurements

Cells were loaded with 5 µM MitoSOX™ red (Invitrogen, M36008) at 37°C for 10 min, protected from light. After the cells were washed twice with 137 mM NaCl, 2.7 mM KCl, 1.8 mM CaCl₂, 1 mM MgCl₂, 0.2 Na₂HPO₄, 12 mM NaHCO₃, 5.5 mM glucose, imaging was carried out using an inverted fluorescence microscope IX83 and the CellSens software (Olympus). MitoSox was excited at 550 nm using the MT20 illumination system (Olympus) with an exposure time of 1 sec. The emitted light was detected via a CCD camera at 570 nm. Images were taken every 2 min for 20 min. The baseline of the fluorescence was measured in the first three images.

Mitotracker-live cell staining

Cells were incubated with Mitotracker (Orange CMTM Ros, M7510, Thermo Fisher, dilution 1:8000) for 15 min. After being washed with PBS, the cells were incubated with Draq5 (DR50050, Biostatus, dilution 1:1000) for 10 min. Cells were fixed and confocal microscopy was performed using the LSM800 (Zeiss).

Western blots

Tissues were lysed in 3.7 M urea, 135 mM TRIS pH 6.8, 1% SDS, 2% NP-40, protease inhibitor cocktail (Roche). Protein extracts were separated by SDS gel electrophoresis and transferred to nitrocellulose membranes. Western blots were performed using the following primary and secondary antibodies: anti-GFP (1:1000, 11814460001, Sigma-Aldrich), anti-GAPDH (1:1000, 2118L, Cell Signaling), anti-IDH3g (1:1000, HPA002017, Sigma-Aldrich), goat anti-rabbit (1:10000, Santa Cruz) and goat anti-mouse (1:1000, Sigma-Aldrich).

PEG switch assay

The PEG switch assay was performed according to a previously described protocol ⁶⁴. In brief, cells were treated with 50 mM D-ala, 50 mM L-ala, 8 mM NAC or 500 µM H₂O₂ respectively. After a washing step with ice-cold PBS containing 20 mM of N-ethylmaleimide (NEM), 150 µL of ice-cold PEG switch lysis buffer containing 1% SDS, 100 mM NEM and 100 mM Tris pH 7.4 were added to the cells. Each lysate was incubated in a shaker at 50 °C and 600 rpm for 25 min to block free thiol groups by alkylation with NEM enriched lysis buffer. While 50 µL from each sample were used as inputs, the rest 100 µL were supplemented with buffer containing 200 mM DTT to reduce oxidized protein thiols. After a 30 min incubation at room temperature, excess DTT was removed using Zeba™ Spin desalting columns (Thermo-Fisher Scientific). After addition of the thiol-labeling buffer containing 70 mM PEG-maleimide (5 kDa; number 63187; Sigma-Aldrich) and 7% SDS in 500 mM Tris pH 7.4, samples were incubated on a laboratory agitator at room temperature for 2 hrs in the dark. Finally, each input and sample was supplemented with 6× reducing Laemmli sample buffer containing 5% β-mercaptoethanol and subjected to Western immunoblot analysis.

RNA quantification

Total RNA was isolated from left ventricles using Trizol (Invitrogen)/chloroform extraction. 1 µg RNA was reverse transcribed into cDNA using the First Strand cDNA Synthesis kit (Thermo-Fischer Scientific) according to the manufacturer's instruction. Quantitative real-time polymerase chain reaction (qRT-PCR) was performed amplifying 1 µL cDNA with SensiMix™ SYBR LoX (Bioline), and 20 pM respective forward and reverse primers in an MX3005Pro light cycler (Agilent). To calculate the relative expression of fold difference in the gene of interest, the ΔΔCT analysis method was used. The murine ribosomal protein S12 (ms12) was used as a reference gene.

The following primers were used **ICAM1** for 5'-CCGTGGGGAGGAGATACTGAGC-3', rev 5'-GGAAGATCGAAAGTCCGGAGGC-3'; **IL-1b** for 5'-AGCTTCAGGCAGGCAGTATCAC-3', rev 5'-AATGGGAACGTACACACCAGC-3'; **TNFa** 5'-GACCCTCACACTCAGATCATCTTC-3', 5'-CCACTTGGTGGTTTGCTACGA-3'; **iNOs** for 5'-AAGTCCAGCCGACACCCT-3', 5'-TCCGTGGCAAAGCGAGCCAG-3'; **NQO1** for 5'-GGTAGCGGCTCCATGTAATCTC-3', rev 5'-CCAGACGGTTTCCAGACGTTTC-3'; **HMOX1** for 5'-GACAGCCCCACCAAGTTCAAAC-3', rev 5'-CCTCTGACGAAGTGACGCCATC-3'; **Srxn1** for 5'-CGGTGCACAACGTACCAATCGC-3', rev 5'-GCAGCCCCCAAAGGAATAGTAG-3'; **Txnrd1** for 5'-GTGGGTTGCATACCTAAGAA-3', rev 5'-GCATTCTCATAGACGACCTT-3'; **Prdx1** 5'-GGCTCGACCTGCTGATAG-3', rev 5'-GCAATGATCTCCGTGGGACA-3'; **Prdx2** for 5'-GGGCATTGCTTACAGGGGTC-3', rev 5'-TGGGCTTGATGGTGTCAGT-3'; **Prdx3** for 5'-GAAGGTTGCTCTGGTCCTCG-3', rev 5'-GGTGTGGAAAGAGGAAGTGGT-3'; **Prdx5** for 5'-CCTTTGGGAAGGCGACAGA-3', rev 5'-CATCTGGCTCCACGTTCACT-3'; **Gpx1** for 5'-CAGTCCACCGTGATGCCTTC-3', rev 5'-TCATTCTTGCCATTCTCCTGGT-3'; **Gpx2** for 5'-CCAGTTCGGACATCAGGAGAA-3', rev 5'-GTCATGAGGGAGAACGGGTC-3'; **Gpx3** for 5'-AGCCAGCTACTGAGGTCTGA-3', rev 5'-GAGGGCAGGAGTTCTTCAGG-3'; **Txn1** for 5'-GCCCTTCTCCATTCCCTCTG-3', Txn1 rev 5'-AGTCTGGCATGCATTGACT-3'; **Txn2** for 5'-TGGACTTTCATGCACAGTGGT-3', rev 5'-TCCCCACAACTGTCCACC-3'; **IDH3a** for 5'-AGGGAAGTTGCGGAGAACTG-3', rev 5'-GGGCTGTTCCATGAACCGAT-3'; **IDH3b** for 5'-GGAAGTGTCAAGGCTGCTG-3', rev 5'-ACGCCTCAGCTGCATATCAT-3'; **IDH3g** for 5'-GCTGCAAAGGCAATGCTCAA-3', rev 5'-GGAGGAATTGTTGTTGTGAGGA-3'; **SDHC** for 5'-AAGATGGCTGCGTTCTTGCT-3', rev 5'-TCCCAAAGGAGCAGCATTTCT-3'; **ms12** for 5'-GAAGCTGCCAAGGCCTTAGA-3', rev 5'-AACTGCAACCAACACCTTC-3'.

Metabolomics analysis

Levels of TCA cycle intermediates (organic acids) in cells were determined by Anion-Exchange Chromatography coupled to Electrospray Ionization High-Resolution Mass Spectrometry (IC-ESI-HRMS) using a procedure previously described⁶⁵ with several modifications: 5 x 10⁶ cells per biological replicate were suspended in 250 µL of ice-cold acetonitrile/methanol/water 2:2:1 (v/v/v) using the Precellys 24 Homogenisator (Bertin Instrumenta) at 6,500 rpm for 10 sec. 100 µL of homogenate were mixed with further 225 µL of acetonitrile/methanol/water 2:2:1 (v/v/v) and 25 µL of a mixture of isotope-labeled internal standard in Milli-Q water (5 µM D4-succinic acid (D4-SUC), Eurisotop). After thorough mixing and centrifugation (16,100 RCF, 5 min, 4 °C), 300 µL of supernatant were dried under reduced pressure. The residue was resolved in 100 µL of Milli-Q water, transferred to autoinjector vials and immediately measured.

IC-HRMS analysis was performed using a Dionex Integrion RFIC system (Thermo Scientific) equipped with a Dionex IonPac AS11-HC column (2 mm × 250 mm, 4 µm particle size, Thermo Scientific) and a Dionex IonPac AG11-HC guard column (2 mm × 50 mm, 4 µm, Thermo Scientific) and coupled to a Q Exactive HF quadrupole-orbitrap mass spectrometer (Thermo Scientific). 5 µL of sample were injected using a Dionex AS-AP at 10°C. The IC was operated at a flow rate of 0.38 mL/min with a potassium hydroxide gradient which was produced by an eluent generator with a potassium hydroxide cartridge and Milli-Q water. The gradient started with 10 mM KOH over 3 min, 10–50 mM from 3 to 12 min, 50–100 mM from 12 to 19 min, held at 100 mM from 19 to 25 min, and re-equilibrated at 10 mM for 3 min. The total run time was 28 min. A Dionex ADRS 600, 2 mm suppressor was operated with 95 mA, and methanol was used to produce a make-up flow at a flow rate of 0.15 mL/min.

The mass spectrometer was operated in the negative ion mode. Full MS scans in the range of m/z 60-900 were acquired with a resolution of 120,000, an Automatic Gain Control (AGC) target value of 1 x 10⁶ and a maximum injection time (IT) of 240 ms. Spectrum data were collected in the centroid mode. The ESI source was operated with flow rates for sheath gas, auxiliary gas, and sweep gas of 50, 14 and 3, respectively. The spray voltage setting was 2.75 kV, the capillary temperature 230 °C, the S-lens RF level 45, and the auxiliary gas heater temperature 380 °C.

The exact m/z traces of the internal standards and endogenous citric acid cycle organic acids were extracted and integrated using Skyline 21.2.0.369 (open-source). Endogenous metabolites were quantified by normalizing their peak areas to those of the D4-SUC as internal standard for organic acids.

Glutathione levels

Glutathione levels were determined using the GSH/GSSG-Glo assay kit (V6611, Promega) according to the manufacturer's instructions.

ATP level measurement by luminescence

ATP levels were determined using the CellTiter-Glo kit (G7570, Promega) according to the manufacturer's instructions.

ATP level measurement by staining and fluorescence microscopy

Cells were washed twice with fresh medium and loaded with 5 µM ATP-Red dye (Merck, SCT045) for 20 min at 37°C. After washing, the cells were excited at 550 nm using an inverted fluorescence microscope IX83, MT20 illumination system (Olympus) with an exposure time of 1 sec. The emitted light was detected via a CCD camera at 570 nm. Fluorescence intensities of the intracellular ATP were calculated by the CellSens software. Generally, 25 regions of interest (ROI) for ATP labelling were selected on three consecutive images. Background was subtracted and the average pixel intensity of each ROI was calculated and extracted from the software. The average fluorescence intensity of each ROI was calculated as the mean value of the ROIs at the three time points. To normalize the data from different experiments, the data of the cells either treated with L-ala or D-ala (F(l), F(d)) was normalized by the data of the cells without any treatment(F(n)) as follows: Ratio = F(l)/F(n) or F(d)/F(n).

Oxygen consumption rate (OCR) and extracellular acidification rate (ECR)

Real-time measurements of OCR and ECR were carried out using the XFe-96 Extracellular Flux Analyzer (Seahorse, Agilent). Cells were plated in XFe-96 plates (Agilent) at the density of 30,000 cells/well. Cells were analyzed 24 hrs after plating. OCR and ECR were measured in XFe media (non-buffered Dulbecco's modified eagle medium (DMEM)) medium, pH-7.4 containing 10 mM XF glucose, 2 mM XF glutamine, 1 mM XF pyruvate under basal conditions and in response to 3.7 µM oligomycin and 1.3 µM of antimycin-A and rotenone (Sigma-Aldrich, St. Louis, MO, USA). OCR, ECR and ATP production from glycolysis and mitochondria were calculated according to the manufacturer's instructions.

Enzyme activity measurements

For determining enzyme activities, the IDH, succinate dehydrogenase (SDH), malate dehydrogenase (MDH), fumarase, aconitase activity assay kits were used according to the manufacturer's recommendation (all Sigma-Aldrich).

Atomistic molecular dynamics simulations

The initial coordinates for the human IDH3a/g dimer with Mg^{2+} , citrate and ADP were taken from the PDB (PDB ID: 5GRE³⁵). Missing residues were fixed with MODELLER⁶⁶ and citrate parameters were generated with the CHARMM general force field (CGenFF) v2.4.0 using the ParamChem web server. Two systems were modelled: the IDH3a/g dimer with Mg^{2+} , citrate and ADP and the same system with a disulfide bond between Cys284 and Cys148 from the g subunit. The protein complexes were set up in a truncated octahedral box containing water and NaCl ions accounting for a concentration of ~20 mM mimicking the mitochondrial matrix milieu. 5 replicas of each system were run for 1 ms each using the CHARMM36m⁶⁷ force field in GROMACS v2019.3⁶⁸. Each system was minimized, heated to 300 K, and equilibrated under NPT conditions using a Nosé-Hoover thermostat^{69,70}, and a Parrinello-Rahman barostat with a compressibility of $4.5 \cdot 10^{-5} \text{ bar}^{-1}$ to a reference pressure of 1 bar. The integration timestep was set to 2 fs, and bonds to hydrogens were constrained with the LINCS algorithm. Long-range electrostatics were computed using particle-mesh Ewald with a mesh size of 0.12 nm; van der Waals interactions were shifted smoothly to zero between 1.0 nm and 1.2 nm.

RMSD analysis was performed with the `gmx rms` tool of Gromacs, and the force distribution analysis (FDA) with the FDA Gromacs tool³⁷ to identify residues that experience differential forces due to the presence of the disulphide bond. In each of the independent simulations, the residue-based pairwise forces (F_{ij} , where j and i are residues) were calculated and the punctual stress (σ_{ij}) averaged over 10 blocks of the trajectory, resulting in total in 50 data points for each setup. To obtain the difference between the systems without (noSS) and with disulfide bridge (SS), we computed the difference between their averages. Student's t test was performed on the two series with 50 datapoints to pinpoint those residues that experience a statistically different force. Residues with a p value below 0.0001 are highlighted in the dimer structure. Statistical tests were performed with scipy's statistical module (scipy.stats v1.5.4). Visualization was performed with VMD v1.9.4a51. For clarity, residues are numbered with the UNIPROT numbering followed by the subunit they belong to.

Quantification and statistical analysis

Statistical analyses for the *in vivo* and *in vitro* experiments were performed using GraphPad Prism software 9.0.0 (GraphPad Software). Two-way ANOVA with Tukey's test was used for the time-course echocardiography analysis and the isometric force measurements when comparing wt and HyPer-DAO mice treated with D-ala or L-ala. One-way ANOVA with Dunnett's test was used for the time course echocardiography analysis when analysing the HyPer-DAO mice in the on/off experiments. One-sample t-test was used for the analysis of the fold change of RNA levels. One-way ANOVA with Bonferroni's test were used to compare enzyme activities, amount of PEGylated IDH3g, ATP levels and relative levels of metabolites. Specific tests were identified in the respective figures. p values and sample size can be found in the figures and the figure legends.

Data availability

The mouse line generated in this study will be deposited to the Knockout Mouse Project (KOMP). Proteomics data are available via ProteomeXchange with identifier PXD033119 (Project DOI: 0.6019/PXD033119).

Declarations

Acknowledgments

This work was funded by the Deutsche Forschungsgemeinschaft (DFG) IRTG1816 and Ka 1269/13-1 to DMK, by Germany's Excellence Strategy - EXC 2067/1-390729940 to PR, TB and the DFG-funded SFB1002 (project A06) to PR. We thank Annette Hillemann and Katja Brechtel-Curth for their expert technical support and Elvina Philip for help with the PEG switch assay.

Author contributions

Experimentation, M.N., A.M.V.L., J.G., G.J.v.B., A.J., A.F.B., S.R., S.B., M.S., J.L., H.W., A.C.; analysis, M.N., A.M.V.L., J.G., A.F.B., R.A.B., C.F., J.B., I.B., J.R., P.R., T.B., V.V.B., D.M.K.; manuscript preparation M.N., M.V.L., J.G., P.R., V.V.B. and D.M.K.; supervision V.V.B. and D.M.K.; funding acquisition D.M.K.. All authors reviewed the manuscript.

Competing interests

The authors declare no competing interests.

Materials & Correspondence

Further information and requests for resources or reagents should be directed to and will be fulfilled by Dörthe M. Katschinski (doerthe.katschinski@med.uni-goettingen.de).

References

1. Jones DP, Sies H. The Redox Code. *Antioxid Redox Signal* **23**, 734–746 (2015).

2. Ryter SW, *et al.* Mechanisms of cell death in oxidative stress. *Antioxid Redox Signal* **9**, 49–89 (2007).
3. Reczek CR, Chandel NS. ROS-dependent signal transduction. *Curr Opin Cell Biol* **33**, 8–13 (2015).
4. Benchoam D, Cuevasanta E, Moller MN, Alvarez B. Hydrogen Sulfide and Persulfides Oxidation by Biologically Relevant Oxidizing Species. *Antioxidants (Basel)* **8**, (2019).
5. Brandes RP, Rezende F, Schroder K. Redox Regulation Beyond ROS: Why ROS Should Not Be Measured as Often. *Circ Res* **123**, 326–328 (2018).
6. Chen X, Lee J, Wu H, Tsang AW, Furdul CM. Mass Spectrometry in Advancement of Redox Precision Medicine. *Adv Exp Med Biol* **1140**, 327–358 (2019).
7. Lennicke C, Rahn J, Heimer N, Lichtenfels R, Wessjohann LA, Seliger B. Redox proteomics: Methods for the identification and enrichment of redox-modified proteins and their applications. *Proteomics* **16**, 197–213 (2016).
8. Groitl B, Jakob U. Thiol-based redox switches. *Biochim Biophys Acta* **1844**, 1335–1343 (2014).
9. Lennicke C, Cochemé HM. Redox metabolism: ROS as specific molecular regulators of cell signaling and function. *Molecular Cell* **81**, 3691–3707 (2021).
10. Swain L, Nanadikar MS, Borowik S, Zieseniss A, Katschinski DM. Transgenic Organisms Meet Redox Bioimaging: One Step Closer to Physiology. *Antioxid Redox Signal* **29**, 603–612 (2018).
11. Ezerina D, Morgan B, Dick TP. Imaging dynamic redox processes with genetically encoded probes. *J Mol Cell Cardiol* **73**, 43–49 (2014).
12. Schwarzlander M, Dick TP, Meyer AJ, Morgan B. Dissecting Redox Biology Using Fluorescent Protein Sensors. *Antioxid Redox Signal* **24**, 680–712 (2016).
13. Lukyanov KA, Belousov VV. Genetically encoded fluorescent redox sensors. *Biochim Biophys Acta* **1840**, 745–756 (2014).
14. Belousov VV, *et al.* Genetically encoded fluorescent indicator for intracellular hydrogen peroxide. *Nat Methods* **3**, 281–286 (2006).
15. Matlashov ME, Belousov VV, Enikolopov G. How much H₂O₂ is produced by recombinant D-amino acid oxidase in mammalian cells? *Antioxid Redox Signal* **20**, 1039–1044 (2014).
16. Hafstad AD, Nabeebaccus AA, Shah AM. Novel aspects of ROS signalling in heart failure. *Basic Res Cardiol* **108**, 359 (2013).
17. Smolyarova DD, Podgorny OV, Bilan DS, Belousov VV. A guide to genetically encoded tools for the study of H₂O₂. *FEBS J*, (2021).
18. Bogdanova YA, Schultz C, Belousov VV. Local Generation and Imaging of Hydrogen Peroxide in Living Cells. *Curr Protoc Chem Biol* **9**, 117–127 (2017).
19. Gloire G, Legrand-Poels S, Piette J. NF-kappaB activation by reactive oxygen species: fifteen years later. *Biochem Pharmacol* **72**, 1493–1505 (2006).
20. Tonks NK. Redox redux: revisiting PTPs and the control of cell signaling. *Cell* **121**, 667–670 (2005).
21. Koitabashi N, Kass DA. Reverse remodeling in heart failure—mechanisms and therapeutic opportunities. *Nat Rev Cardiol* **9**, 147–157 (2011).
22. Aldini G, *et al.* N-Acetylcysteine as an antioxidant and disulphide breaking agent: the reasons why. *Free Radic Res* **52**, 751–762 (2018).
23. Ezerina D, Takano Y, Hanaoka K, Urano Y, Dick TP. N-Acetyl Cysteine Functions as a Fast-Acting Antioxidant by Triggering Intracellular H₂S and Sulfane Sulfur Production. *Cell Chem Biol* **25**, 447–459 e444 (2018).
24. Cox AG, Winterbourn CC, Hampton MB. Mitochondrial peroxiredoxin involvement in antioxidant defence and redox signalling. *Biochem J* **425**, 313–325 (2009).
25. Dang L, Su SM. Isocitrate Dehydrogenase Mutation and (R)-2-Hydroxyglutarate: From Basic Discovery to Therapeutics Development. *Annu Rev Biochem* **86**, 305–331 (2017).
26. Lee SH, *et al.* Role of NADP⁺-dependent isocitrate dehydrogenase (NADP⁺-ICDH) on cellular defence against oxidative injury by gamma-rays. *Int J Radiat Biol* **80**, 635–642 (2004).
27. Koh HJ, *et al.* Cytosolic NADP⁺-dependent isocitrate dehydrogenase plays a key role in lipid metabolism. *J Biol Chem* **279**, 39968–39974 (2004).
28. Ramachandran N, Colman RF. Chemical characterization of distinct subunits of pig heart DPN-specific isocitrate dehydrogenase. *J Biol Chem* **255**, 8859–8864 (1980).
29. May JL, *et al.* IDH3alpha regulates one-carbon metabolism in glioblastoma. *Sci Adv* **5**, eaat0456 (2019).
30. Pak VV, *et al.* Ultrasensitive Genetically Encoded Indicator for Hydrogen Peroxide Identifies Roles for the Oxidant in Cell Migration and Mitochondrial Function. *Cell Metab* **31**, 642–653 e646 (2020).
31. Hoehne MN, *et al.* Spatial and temporal control of mitochondrial H₂O₂ release in intact human cells. *EMBO J*, e109169 (2022).
32. Yoo HC, Yu YC, Sung Y, Han JM. Glutamine reliance in cell metabolism. *Exp Mol Med* **52**, 1496–1516 (2020).
33. Xiao H, *et al.* A Quantitative Tissue-Specific Landscape of Protein Redox Regulation during Aging. *Cell* **180**, 968–983 e924 (2020).
34. Craig DB, Dombkowski AA. Disulfide by Design 2.0: a web-based tool for disulfide engineering in proteins. *BMC Bioinformatics* **14**, 346 (2013).
35. Ma T, Peng Y, Huang W, Ding J. Molecular mechanism of the allosteric regulation of the alphasubunit heterodimer of human NAD-dependent isocitrate dehydrogenase. *Sci Rep* **7**, 40921 (2017).
36. Ma T, Peng Y, Huang W, Liu Y, Ding J. The beta and gamma subunits play distinct functional roles in the alpha2betagamma heterotetramer of human NAD-dependent isocitrate dehydrogenase. *Sci Rep* **7**, 41882 (2017).
37. Costescu BI, Grater F. Time-resolved force distribution analysis. *BMC Biophys* **6**, 5 (2013).
38. Sun P, Liu Y, Ma T, Ding J. Structure and allosteric regulation of human NAD-dependent isocitrate dehydrogenase. *Cell Discov* **6**, 94 (2020).
39. Sies H, *et al.* Defining roles of specific reactive oxygen species (ROS) in cell biology and physiology. *Nature Reviews Molecular Cell Biology*, (2022).
40. Sies H, Jones DP. Reactive oxygen species (ROS) as pleiotropic physiological signalling agents. *Nature Reviews Molecular Cell Biology* **21**, 363–383 (2020).
41. van der Reest J, Lilla S, Zheng L, Zanivan S, Gottlieb E. Proteome-wide analysis of cysteine oxidation reveals metabolic sensitivity to redox stress. *Nature Communications* **9**, 1581 (2018).

42. Chouchani ET, *et al.* Ischaemic accumulation of succinate controls reperfusion injury through mitochondrial ROS. *Nature* **515**, 431–435 (2014).
43. Steinhorn B, Sorrentino A, Badole S, Bogdanova Y, Belousov V, Michel T. Chemogenetic generation of hydrogen peroxide in the heart induces severe cardiac dysfunction. *Nat Commun* **9**, 4044 (2018).
44. Spyropoulos F, *et al.* Metabolomic and transcriptomic signatures of chemogenetic heart failure. *Am J Physiol Heart Circ Physiol* **322**, H451–H465 (2022).
45. Braginski JE, Franzen JS, Chung AE. Reversible inactivation of *Azotobacter vinelandii* TPN⁺ -isocitrate dehydrogenase by the formation of an intramolecular disulfide bridge. *Biochem Biophys Res Commun* **38**, 644–650 (1970).
46. Munoz-Vargas MA, Gonzalez-Gordo S, Canas A, Lopez-Jaramillo J, Palma JM, Corpas FJ. Endogenous hydrogen sulfide (H₂S) is up-regulated during sweet pepper (*Capsicum annuum* L.) fruit ripening. In vitro analysis shows that NADP-dependent isocitrate dehydrogenase (ICDH) activity is inhibited by H₂S and NO. *Nitric Oxide* **81**, 36–45 (2018).
47. Niazi AK, *et al.* Cytosolic Isocitrate Dehydrogenase from *Arabidopsis thaliana* Is Regulated by Glutathionylation. *Antioxidants (Basel)* **8**, (2019).
48. Nietzel T, Mostertz J, Hochgrafe F, Schwarzlander M. Redox regulation of mitochondrial proteins and proteomes by cysteine thiol switches. *Mitochondrion* **33**, 72–83 (2017).
49. Sena Laura A, Chandel Navdeep S. Physiological Roles of Mitochondrial Reactive Oxygen Species. *Molecular Cell* **48**, 158–167 (2012).
50. Mailloux RJ, Jin X, Willmore WG. Redox regulation of mitochondrial function with emphasis on cysteine oxidation reactions. *Redox Biol* **2**, 123–139 (2014).
51. Tretter L, Adam-Vizi V. Alpha-ketoglutarate dehydrogenase: a target and generator of oxidative stress. *Philos Trans R Soc Lond B Biol Sci* **360**, 2335–2345 (2005).
52. Gardner PR. Aconitase: sensitive target and measure of superoxide. *Methods Enzymol* **349**, 9–23 (2002).
53. Mailloux RJ, McBride SL, Harper ME. Unearthing the secrets of mitochondrial ROS and glutathione in bioenergetics. *Trends Biochem Sci* **38**, 592–602 (2013).
54. Mailloux RJ, Willmore WG. S-glutathionylation reactions in mitochondrial function and disease. *Front Cell Dev Biol* **2**, 68 (2014).
55. Vujic A, Koo ANM, Prag HA, Krieg T. Mitochondrial redox and TCA cycle metabolite signaling in the heart. *Free Radic Biol Med* **166**, 287–296 (2021).
56. Chen CL, Zhang L, Jin Z, Kasumov T, Chen YR. Mitochondrial redox regulation and myocardial ischemia-reperfusion injury. *Am J Physiol Cell Physiol* **322**, C12–C23 (2022).
57. Calabrese G, Morgan B, Riemer J. Mitochondrial Glutathione: Regulation and Functions. *Antioxid Redox Signal* **27**, 1162–1177 (2017).
58. Bolli R, Marban E. Molecular and cellular mechanisms of myocardial stunning. *Physiol Rev* **79**, 609–634 (1999).
59. Heusch G. Myocardial stunning and hibernation revisited. *Nature Reviews Cardiology* **18**, 522–536 (2021).
60. Swain L, *et al.* Redox Imaging Using Cardiac Myocyte-Specific Transgenic Biosensor Mice. *Circ Res* **119**, 1004–1016 (2016).
61. Jatho A, *et al.* Precisely Tuned Inhibition of HIF Prolyl Hydroxylases Is Key for Cardioprotection After Ischemia. *Circ Res* **128**, 1208–1210 (2021).
62. Chen X, *et al.* Discovery of Heteroaromatic Sulfones As a New Class of Biologically Compatible Thiol-Selective Reagents. *ACS Chem Biol* **12**, 2201–2208 (2017).
63. Ermakova YG, *et al.* Red fluorescent genetically encoded indicator for intracellular hydrogen peroxide. *Nat Commun* **5**, 5222 (2014).
64. Burgoyne JR, Oviosu O, Eaton P. The PEG-switch assay: a fast semi-quantitative method to determine protein reversible cysteine oxidation. *J Pharmacol Toxicol Methods* **68**, 297–301 (2013).
65. Schwaiger M, Rampler E, Hermann G, Miklos W, Berger W, Koellensperger G. Anion-Exchange Chromatography Coupled to High-Resolution Mass Spectrometry: A Powerful Tool for Merging Targeted and Non-targeted Metabolomics. *Anal Chem* **89**, 7667–7674 (2017).
66. Fiser A, Do RK, Sali A. Modeling of loops in protein structures. *Protein Sci* **9**, 1753–1773 (2000).
67. Huang J, *et al.* CHARMM36m: an improved force field for folded and intrinsically disordered proteins. *Nat Methods* **14**, 71–73 (2017).
68. Abraham MJ, *et al.* GROMACS: High performance molecular simulations through multi-level parallelism from laptops to supercomputers. *SoftwareX* **1–2**, 19–25 (2015).
69. Nosé S. A molecular dynamics method for simulations in the canonical ensemble. *Molecular Physics* **52**, 255–268 (1984).
70. Hoover WG. Canonical dynamics: Equilibrium phase-space distributions. *Phys Rev A* **31**, 1695–1697 (1985).

Figures

Figure 1

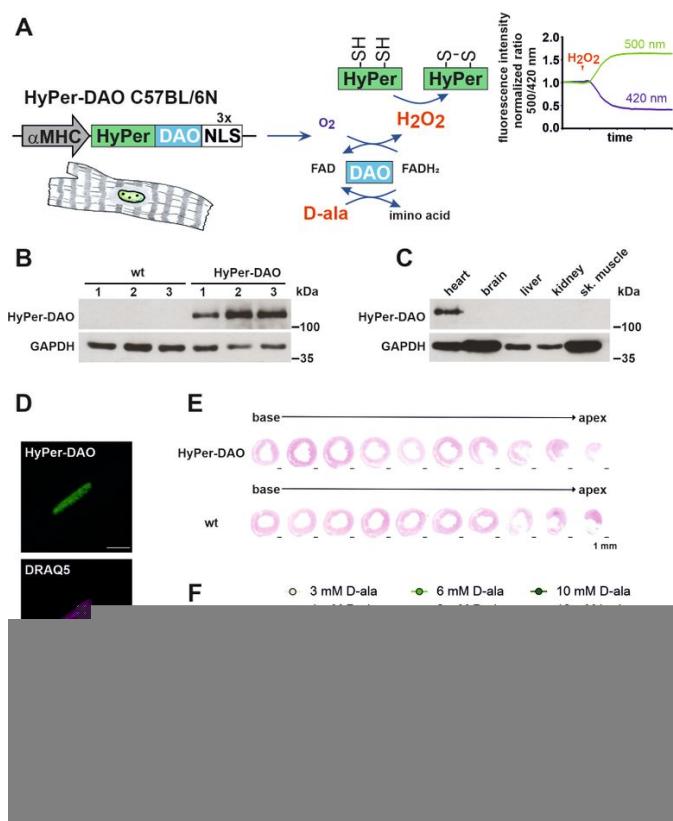


Figure 1

Expression and activation of the HyPer-DAO fusion protein in cardiomyocyte-specific transgenic mice

(A) Scheme of the HyPer-DAO construct used for generating HyPer-DAO cardiomyocyte-specific transgenic mice and the HyPer and DAO chemical reactions. (B) Immunoblot for HyPer-DAO and GAPDH protein levels in cardiac protein lysates from three wild type (wt) and three HyPer-DAO mice. (C) Cardiac-specific HyPer-DAO protein expression in a HyPer-DAO mouse as demonstrated by immunoblot performed with protein lysates from different organs. (D) Representative confocal image of a DRAQ5 stained cardiomyocyte isolated from a HyPer-DAO mouse. (E) HE stained sections of hearts obtained from one HyPer-DAO and one wt mouse. (F) Response of HyPer-DAO cardiomyocytes to treatment with D-ala or L-ala. The HyPer fluorescence response was recorded in the cytosol (left panel) and the nucleus (right panel). Ratios are normalized to the HyPer ratio prior to treatment, 13-25 cardiomyocytes per condition were analyzed. mean \pm SEM.

Figure 2

Reversible impaired inotropic response of HyPer-DAO mice towards activation of DAO

Relative changes in (A) RNA levels of NF- κ B (left panel) and Nrf2 (right panel) target genes and (B) antioxidant enzymes in the heart of HyPer-DAO male mice versus wild type (wt) male mice after 7 or 21 days of treatment with 55 mM D-ala in the drinking water. n = 3-4 mice per group. (C, D) Echocardiographic analysis of fractional area shortening (FAS), ejection fraction (EF), anterior wall thickness (AWth) and posterior wall thickness (PWth) in male (in C) and a mixed group of female and male (in D) HyPer-DAO or wt mice after treatment with 55 mM D-ala or L-ala in the drinking water as indicated. (E) Quantification of Sirius red staining for fibrotic areas in cardiac slices of male HyPer-DAO and wt mice. The total area of fibrosis (t), interstitial (i) and perivascular (p) fibrotic area were quantified in the left ventricles. Cardiac slices of mice that underwent transverse aortic constriction (TAC) or sham surgery were used as positive control for the staining and quantification. n = 3-5 mice per group. (F) Heart slices isolated from a mixed group of male/female HyPer-DAO or wt mice were treated with 0-10 mM D-ala +/- 1 mM NAC and force development was measured. mean \pm SEM, *p<0.05, **p<0.01 by one sample t-test (A and B), one-way ANOVA (D and E) or two-way ANOVA (C and F). This figure is related to Supplemental Fig. 1.

Figure 3

IDH3g is redox modified in the hearts of HyPer-DAO mice after activation of DAO *in vivo*

(A) Scheme of the redox proteomics analysis performed with heart samples obtained from male HyPer-DAO (n = 3) and wt mice (n = 3) that were treated for 7 days with 55 mM D-ala in the drinking water. (B) Volcano plot of the proteins identified in the redox proteomics experiment as outlined in A. Green and red dots indicate proteins with significantly increased and decreased redox modification in the HyPer-DAO hearts compared to wt hearts, respectively. Signal to noise ratio, STN (C) Protein dendrogram for the different murine isocitrate dehydrogenase isoforms and subunits. (D) Activity of the indicated TCA cycle enzymes determined in protein extracts obtained from hearts of 7 days D-ala treated female HyPer-DAO and wt mice. n = 6 mice per group. (E) Relative changes in RNA levels of IDH3 subunits in the heart of HyPer-DAO mice versus wt mice after 7 and 21 days of treatment with D-ala. n = 3 mice per group (F) Immunoblot for IDH3g and vinculin protein levels in heart samples of three HyPer-DAO and three wt mice after 7 days of treatment with D-ala. (G) IDH3 activity in samples obtained from hearts of a mixed group of male and female HyPer-DAO or wt mice after 7 days treatment with D-ala or after 7 days treatment with D-ala plus 2 additional D-ala free days (OFF). n = 7-19 mice per group. (H) IDH1/2 and IDH3 activity in protein samples obtained from isolated HyPer-DAO cardiomyocytes non-treated (n.t.) and after treatment with 2 mM D-ala or L-ala for 20 min. Cardiomyocytes were isolated from n = 7-8 mice per group in independent experiments. mean ± SEM. *p<0.05, by unpaired t-test (D), one-sample t-test (E), and one-way ANOVA (G and H).

Figure 4

HyPer-DAO overexpressing HEK cells exhibit a reversible redox modification and activity of IDH3 after activation of DAO *in vitro*

(A) Confocal images of HEK cells overexpressing the HyPer-DAO fusion protein in the nucleus (HyPer-DAO NLS), the cytoplasm (HyPer-DAO NES) or the mitochondrial matrix (HyPer-DAO MLS) after the indicated staining. (B) HyPer fluorescence response in HyPer-DAO overexpressing HEK cells to treatment with L-ala, D-ala or H₂O₂. Ratios are normalized to the HyPer ratio prior to the stimulation, 25-30 cells per condition were analyzed, see also supplemental Fig. 2. (C) IDH3 activity in cell extracts obtained from HEK HyPer-DAO NES, HEK HyPer-DAO NLS and HEK HyPer-DAO MLS cells non-treated (n.t.) and after treatment with 50 mM D-ala, 50 mM L-ala ± 8 mM NAC or 500 μM H₂O₂ for 20 min. n = 6-8 independent experiments, see also supplemental Fig. 3. (D) HyPer fluorescence (left panel) and MitoSOX (right panel) response in HyPer-DAO NLS cells to treatment with L-ala, D-ala ± NAC. Ratios are normalized to the HyPer ratio or the MitoSOX fluorescence prior to the stimulation, 30 cells per condition were analyzed. (E) Quantification of IDH3g oxidation analyzed by PEG switch assay in HEK HyPer-DAO NLS cells n.t. and after treatment with 50 mM L-ala, 50 mM D-ala or 500 μM H₂O₂ for 20 min. n = 3 independent experiments. A representative experiment is shown in the left panel. (F) IDH1/2 and IDH3 activity in cell extracts obtained from HEK HyPer-DAO NLS cells n.t. and after 50 mM D-ala for 20 min or 50 mM D-ala for 20 min and additional 24 hrs D-ala free incubation time. n = 5-6 independent experiments. (G) Quantification of IDH3g oxidation analyzed by PEG switch assay in HEK HyPer-DAO NLS cells n.t. and after treatment with 50 mM D-ala ± 8 mM NAC for 20 min or 50 mM D-ala for 20 min and an additional 30 min D-ala free incubation time. n = 5 independent experiments. Representative experiment is shown in the left panel. mean ± SEM, *p<0.05, **p<0.01 by one-way ANOVA (D, E, F and G).

Figure 5

Endogenously produced H₂O₂ impairs ATP produced in the mitochondria

(A) ATP levels in HEK HyPer-DAO NLS cells either non-treated (n.t.) or after treatment with 50 mM L-ala and D-ala ± 8 mM NAC or 500 μM H₂O₂ for 20 min, n = 8 independent samples. (B) Mitochondrial and glycolytic ATP production in HEK HyPer-DAO NLS cells after treatment with 50 mM L-ala or D-ala for 20 min. n = 4 independent experiments. see also supplemental Fig. 4. (C) Mitochondrial and glycolytic ATP production in cardiomyocytes isolated from HyPer-DAO mice after treatment with 2 mM L-ala or D-ala for 20 min. n = 7 mice per group. (D) TCA cycle metabolite levels in HEK HyPer-DAO NLS cells either non-treated (-) and after treatment with 50 mM L-ala (L) or D-ala (D) for 20 min. n = 6 independent samples per condition. (E) Schematic of the TCA cycle. Metabolites that were found to be significantly increased, after D-ala treatment compared to non-treated or L-ala treatment are indicated in green. (F) Ratio of reduced glutathione (GSH) to oxidized glutathione (GSSG) and total glutathione levels (G) in HEK HyPer-DAO NLS cells either n.t. and after treatment with 50 mM L-ala or D-ala for 20 min, n = 3 independent samples. mean ± SEM (except D), Box-Whisker-Plot in D, *p<0.05, **p<0.01 by one-way ANOVA (A, B, C, D, F and G).

Figure 6

Disulfide bridge formation between IDH3g Cys148 and Cys284 changes the tetramerization interface of IDH3

(A) Quantification of IDH3g Cys148 and Cys333 oxidation as the percentage of occupancy from five 16-week-old male C57BL/6J mice. Data are obtained from the Oximouse database. mean \pm SEM. (B) Structure of the IDH3a/g dimer with main functional sites. Citrate, Mg^{2+} and ADP are shown as ball and sticks. (C) Root mean square deviation (RMSD) plot for the clasp region for each system/replica. (D) Selected clasp regions from the two simulations showing substantial conformational changes (noSSr2, noSSr5, in blue for a subunit and red for g subunit) and one stable reference (SSr2, in cyan for a subunit and orange for g subunit) superimposed onto the tetrameric structure of IDH3 (IDH3a/g / IDH3a/b, PDB ID: 7CE3, clasp regions in grey). For clarity, the zoomed images do not show the IDH3a/b dimer. (E) Stress difference plot. Residues were renumbered consecutively from 0. Regions with statistically relevant changes in the total stress between noSS and SS are highlighted and mapped onto the structure. Cysteines involved in the disulfide bond are circled in yellow. This figure is related to Supplemental Fig. 5.

Figure 7

Redox modification of IDH3g Cys148 and Cys284 is responsible for ATP production in the mitochondria

IDH1/2 (A) and IDH3 (B) activity in cell extracts obtained from HEK HyPer-DAO NLS wild type (wt), HEK HyPer-DAO C148A, HEK HyPer-DAO C284A and HEK HyPer-DAO C236A cells non-treated (n.t.) and after treatment with 50 mM D-ala or 50 mM L-ala for 20 min, n = 6-12 independent experiments per condition. (C) IDH3g oxidation analyzed by PEG switch assay in HEK HyPer-DAO NLS wt, HEK HyPer-DAO Cys148A and HEK HyPer-DAO Cys284A cells n.t. or after treatment with 50 D-ala for 10 min. (D) Mitochondrial and glycolytic ATP production in HEK HyPer-DAO NLS wt and HEK HyPer-DAO C148A cells after treatment with 50 mM L-ala or 50 mM D-ala for 20 min. n = 7 independent experiments. (E) Mitochondrial ATP levels determined with the fluorescence sensor ATP-red in HEK HyPer-DAO NLS wt, HEK HyPer-DAO C148A, HEK HyPer-DAO C284A and HEK HyPer-DAO C236A cells n.t. and after treatment with 50 mM L-ala or 50 mM D-ala for 20 min. In each cell line four independent experiments were performed. 100 cells were analyzed per condition. (F) TCA cycle metabolite levels in HEK HyPer-DAO NLS wt and HEK HyPer-DAO C148A cells non-treated (-) or after treatment with 50 mM L-ala (L) or 50 mM D-ala (D) for 20 min. n = 5 independent samples per condition. (G) Total glutathione levels in HEK HyPer-DAO NLS and HEK HyPer-DAO C148A cells n.t. and after treatment with 50 mM L-ala or D-ala for 3 hrs. n = 7 independent samples. mean \pm SEM (except F), Box-Whisker-Plot in F, *p<0.05, **p<0.01 by one-way ANOVA (A, B, D, E, F and G).

Supplementary Files

This is a list of supplementary files associated with this preprint. Click to download.

- [Supplementaryinformation.pdf](#)